Preprint Cambridge Centre for Computational Chemical Engineering ISSN 1473 – 4273

HRTEM study of soot particles produced by the non-premixed combustion of liquid fuels

Maria Botero [1], Dongping Chen [1], Silvia Gonzáles Calera [1], David Jefferson [2], Markus Kraft [1,3]

released:

[1] Department of Chemical Engineering and Biotechnology
University of Cambridge
New Museums Site
Pembroke Street
Cambridge, CB2 3RA
United Kingdom
E-mail: mk306@cam.ac.uk

[2] Department of Chemistry
University of Cambridge

[3] School of Chemical and Biomedical Engineering
Nanyang Technological University
62 Nanyang Drive
637459
Singapore

Preprint No. 155

UNIVERSITY OF CAMBRIDGE

Keywords: soot, high resolution electron microscopy, simulated TEM, lattice-fringe analysis

Edited by
Computational Modelling Group
Department of Chemical Engineering and Biotechnology
University of Cambridge
New Museums Site
Pembroke Street
Cambridge CB2 3RA
United Kingdom

Fax: + 44 (0)1223 334796
E-Mail: c4e@cam.ac.uk
World Wide Web: http://como.cheng.cam.ac.uk/

Abstract

In this paper the morphology and nanostructure of soot particles as a function of fuel type in a laminar diffusion flame were studied. The fuels considered were heptane, toluene, the volumetric mixture 50% heptane - 50% toluene and a commercial gasoline. The structural features of soot sampled at different positions in the flame were inferred using HRTEM. An image analysis algorithm was developed to calculate the fringe length, tortuosity and inter-fringe spacing from HRTEM images. To assess the performance of the algorithm, simulated TEM images were artificially generated from stacks of polycyclic aromatic hydrocarbons (PAHs). The fringe analysis was performed on the simulated TEM. A good agreement between the fringe image analysis and the known sizes of the molecules and their separation. Primary particles as small as 6 nm were detected in the inception region of the heptane flame, growing to sizes as large as 60 nm in all the flames. Strong oxidation was observed close to the tip in all the flames, affecting mainly the fringe length and, to a lesser extent, the curvature and inter-fringe spacing. Overall, temperature and fuel aromaticity were found to have a great influence in the nanostructure of soot. Toluene exhibits the largest degree of graphitisation. Heptane develops a similar degree of order as the aromatic flames but presents stronger soot oxidation at the tip that reduces the fringe length and increases the highly tortuous fringes. The main differences in the nanostructure of the soot sampled from different flames was the arrangement and degree of order of the PAHs within each particle.

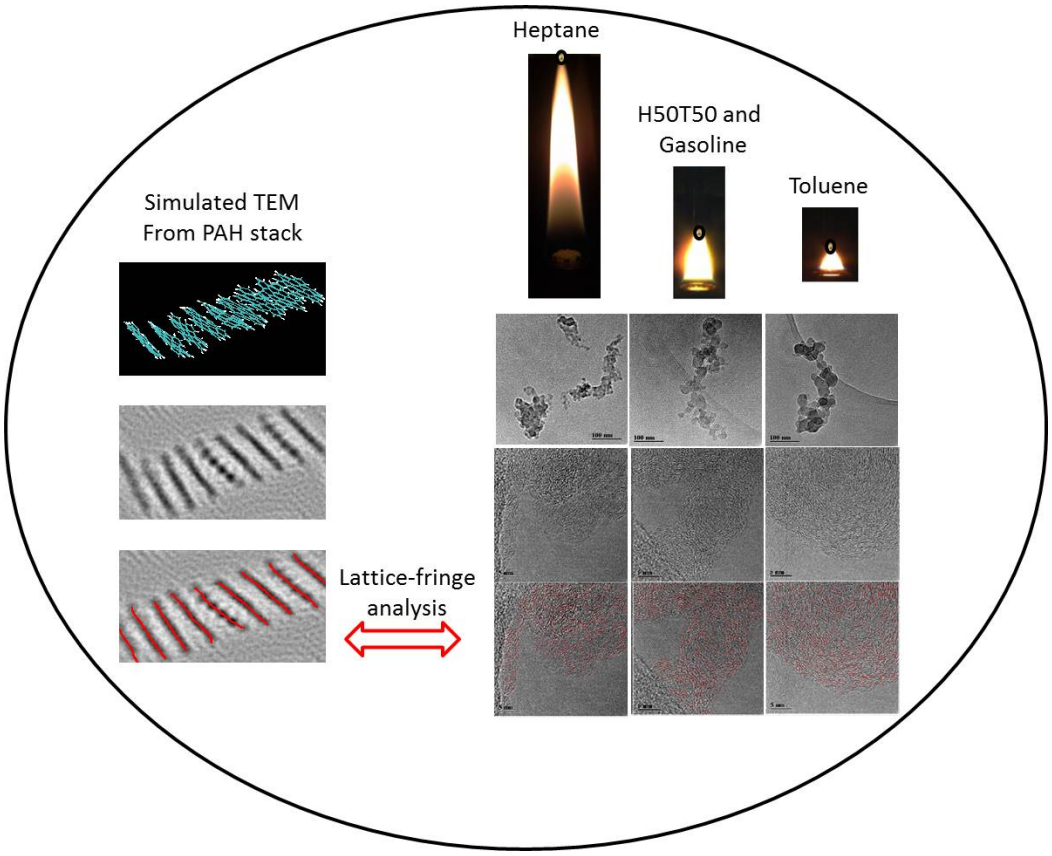

1 Introduction

The last century saw significant efforts to understand the mechanisms of soot formation [7, 23, 24]. However, there is still a gap in the understanding of soot inception and the mechanisms of particle growth and oxidation under different flame environments [40]. Furthermore, the influence of fuel composition on the structure of soot is not yet fully understood. In the last decade great efforts have been made to understand such processes experimentally [4, 43, 54] as well as to model and predict them [13, 50, 56, 62].

Significant contributions have been made towards understanding the smoking process of some hydrocarbons and their mixtures have been made recently [21, 38], showing that soot formation has a strong correlation with the chemical structure of the hydrocarbon fuel. The aromatic content of the fuel has been shown to be largely responsible for the formation of soot particles [34, 35]. One of the quantities that has been used to assess the sooting propensity of a fuel is the threshold sooting index (TSI) [12] that is based on the smoke point (SP) [8] which describes the height above which a flame emits soot. However, no information on the characteristics of the soot particles is available via this property, and experimental data on this matter remain scarce.

Transmission electron microscopy (TEM) has long been applied as a tool to analyse soot particles [20, 32, 44, 57]. More recently, high resolution transmission electron microscopy (HRTEM) has enabled the detailed observation of the structure of the particles. Observation of the atomic columns and the arrangement of the molecules within the particles allows compositional and crystallographic information to be obtained.

Experimental studies of soot morphology revealed that mature particles are microcrystalline near the outer edge, but amorphous in the core [18, 31, 57]. It is clear from these studies that polycyclic aromatic hydrocarbons (PAH) molecules act as a soot precursor, and that their relative orientations decide the crystalline (graphite-like) or amorphous nature of the soot particles. The variations in the structure of the PAHs, their sizes and their orientation in the soot particles has also been found to depend heavily on the type of fuel, the flow rate of the fuel and the temperature [4, 5]. The presence of PAH stacks and clusters revealed by HRTEM images of soot particles, indicates that coagulation of PAHs may be responsible for soot nucleation [30, 61].

The nanostructure of any soot particle reflects on its nucleation and growth history. In general, young soot is amorphous consisting of very disordered and short carbons layers. The maturation process is accompanied by an increase of the structural order. Large, extended lamellae and shorter inter-layer spacing are indicative of a more graphitic and mature structure. Curvature, often expressed as tortuosity, is only relevant in non-planar lamella, and is related to the presence of C5 rings. The C5 rings allow the formation of curved carbon lamella and are necessary for the formation of fullerenes and fullerenic structures [47]. Pyrolysis experiments using indene suggest that the presence of five-membered rings does indeed lead to positive curvature of the graphene layers [58]. It has being suggested that the presence of C5 carbon rings, as well as other non-six-membered rings can explain the resistance of soot to graphitisation [28].

The chemical structure of the fuel also plays an important role in the nanostructure of soot. Young soot formed from light unsaturated hydrocarbons exhibits a poorly ordered

nanostructure, with a progressive increase in structural order with soot maturation. Young soot formed from cyclic paraffins and aromatics tends to have a more organised structure. [4]. This has been explained by the flame environment containing a higher concentration of benzene compared to aliphatic flames. Also, the small content of light hydrocarbons avoids their “intrusion" on the particle nucleus, limiting the disordering of the young soot structure [49].

The effect of temperature on soot nanostructure has been studied [5, 58]. Relatively low temperatures may cause many potential growth sites to be inactive and certain molecular orientations at active (radical) sites may be inhibited based on energetics. The result is a very amorphous soot [58]. Soot carbonisation is observed at high flame temperatures [5]. The higher temperatures favour the decomposition of PAHs into smaller species and correlate with higher concentrations of gas phase hydrogen, acetylene and diacetylene. Here C_2H_2 may be the dominant growth species. Mass growth by a smaller molecular species such as C2 may facilitate the formation of more ordered graphene layers, and more surface sites may be activated [58].

The aim of this investigation is to elucidate the evolution of the nanostructure of soot particles formed in a diffusion flame and to investigate the influence of the fuel composition in order to gain a better understanding of inception and growth processes of soot in such environments. Additionally, the general interpretation of HRTEM images of soot is addressed through the simulation of TEM images from previously optimised clusters of PAHs of known geometries [14, 15, 17, 56]. A series of non-premixed flames of heptane, toluene, an iso-volumetric heptane-toluene mixture and a commercial gasoline were sampled at different flame heights. Soot samples were analysed using an in-house lattice-fringe analysis code. Starting from literature approaches [46, 65], the HRTEM image analysis algorithm was developed and implemented using MATLAB [39]. The performance of the code was tested with the simulated TEM images.

2 Experimental methodology

In this study, a wick-fed burner [8, 63] was used to investigate a laminar diffusion flame of liquid fuels. The burner consists of a cylindric reservoir, with an inner concentric hole where the wick is placed.

2.1 Soot sampling

The soot was sampled inside the flame using a fast insertion technique as depicted in **Figure 1**. Soot particles are driven thermophoretically to the cold wall of the TEM sampling grid held by the probe and are ultimately captured on the surface [20]. The insertion system was calibrated with a fast speed camera. The residence time of the probe was adjusted within the range 53 ms - 250 ms to suit the sooting level at each sample point in each flame. Ten seconds were allowed between insertions to let the grid cool down. Sampling grids were special carbon-supported 3.05 mm diameter TEM grids (300 mesh carbon coated standard square copper grids).

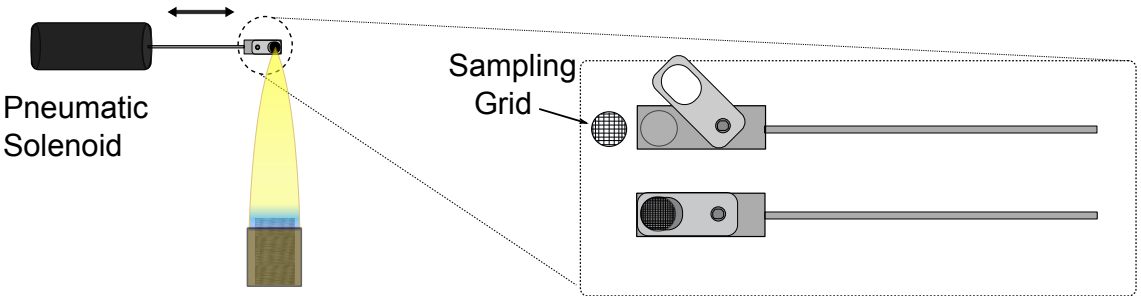

Figure 1: *Sampling systems for particle size analysis.*

The fuels investigated were heptane, toluene, an iso-volumetric heptane-toluene mixture (H50T50) and a commercial gasoline. The gasoline has an aromatic content of approximately 44% by mass (detailed composition data can be found in **Table 1**), and a smoke point very similar to that of H50T50. The flame heights were chosen to be below the smoke point, for toluene 7 mm, H50T50 11 mm, gasoline 11 mm and heptane 40 mm. The sampling points for each flame are depicted in **Figure 2**.

Fuel type	**% mass**
Aromatics	43.8
toluene	*14*
alkyl-benzenes	*29.7*
naphthalenes	*0.14*
Paraffins	44.7
straight	*6.6*
branched	*35.6*
cyclic	*2.5*
Olefins	11
Other	0.47

Table 1: *Chemical composition of commercial gasoline obtained from GC-MS (gas chromatography - mass spectrometry).*

Low and high-resolution TEM images were taken using a JEOL 3011 microscope with and operating voltage of 300 keV using a Lab6 filament. For the lattice-fringe analysis, at least 10 images were acquired in different regions of the grid (5-10 squares surrounding the grid centre) obtained at different magnification (500,000$\times$ and 600,000$\times$). The average primary particle size was determined by measuring the diameter of more than 200 particles for each sample, using the image processing and analysis software ImageJ® to analyse TEM images obtained under 15,000$\times$ magnification. The error in the primary particle measurement is estimated to be $\pm$0.5 nm. All the particle size data was log-normally distributed. The average primary particle size was extracted from the raw data. However, fitted distributions are plotted for the purpose of communicating our observations (only to guide the eye).

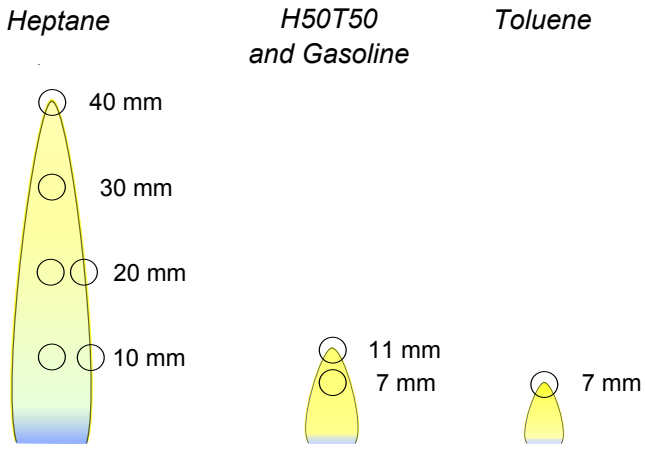

Figure 2: *TEM sampling points in heptane, H50T50, gasoline and toluene flames.*

3 Image Analysis

For almost two decades, most of the HRTEM image analysis was performed using closed-source software where there is no control over the operators that transform the digital image [4, 22, 45, 48, 53, 59, 60]. This made the comparison of different images challenging. Recently lab-made algorithms were introduced, enabling the manipulation and setting of the image processing operators to achieve better control of the resulting image [46, 55, 65]. Some of these algorithms are implemented in MATLAB and apply essentially the same image transformations as other closed-source software, but can be customised depending on the specific need of the raw image.

In this study, we have implemented an algorithm in MATLAB, based on the algorithm presented by Yehliu et al. [65]. The soot nanostructure, including fringe length, tortuosity, and interlayer spacing, was investigated.

The lattice-fringe analysis performed in this paper contains the following steps for image processing: 1- region of interest selection, 2- contrast enhancement using histogram equalisation, 3- gaussian low-pass filter, 4- bottom-hat transformation, 5- binarisation using Otsu's method, 6- skeletonisation, 7- elimination of isolated pixels and pixels with more than 3 connections. A detailed description of the algorithm can be found in the **Appendix A**.

The fringe length is calculated as the number of pixels contained by the fringe multiplied within the length of a pixel (in the case of diagonal pixels the length is calculated as $\sqrt{2}$ times the pixel size). All fringes shorter than 0.483 nm (two aromatic rings) are discarded as unrealistic. Fringe tortuosity is defined as the ratio between fringe length and the fringe linear length (the Euclidean distance between the two end points of the fringe). The calculation of inter-fringe spacing was automated taking into account the fringe orientation. Only inter-fringe separations larger than 0.3354 nm (002 graphite distance) and smaller than 0.6 nm (after which van der waals forces are negligible)[4, 5] were selected.

The values of the operators used in the image analysis are presented in **Table 2**. The operators were the same for all the experimental images. The error in the estimated fringe parameters depends on the pixel size, in our case always less than 0.05 nm.

Table 2: *Operators used for the lattice-fringe analysis of experimental and simulated TEM images.*

	Histogram Equalisation (discrete gray levels)	Gaussian filter size (pixels)	Gaussian filter deviation (1/pixels)	Morphological closing element size (disk element)	Spatial resolution (nm/pixel)
Simulated HBC stack	64	40	11	45	0.0052
Simulated Coronene cluster	64	15	5	7	0.0092
Experimental (600,000x)	5	7	3	2	0.0595
Experimental (500,000x)	5	7	3	2	0.0704

3.1 Simulated TEM testing of the fringe analysis algorithm

Simulated TEM images were produced using the TEMSIM package [33] which applies a multi-slice method to simulate the electron scattering. This package has been used to reveal the structure of a variety of materials [26, 41, 42, 51]. In the multi-slice method, the sample is divided into equal-sized slices, each of which is thin enough to be approximated as a simple phase shift of the electron beam. In this work, we used 0.35 nm as the layer separation of the PAH stack in the imaging simulation. It was found that the simulated TEM images were insensitive to this parameter. Details on the parameters used in the TEMSIM package can be found in the **Appendix B**.

4 Results and Discussion

4.1 Simulated TEM test

To test the fringe analysis algorithm, TEM images were simulated from clusters of PAHs obtained from previous MD simulations [15, 17, 56]. The length of the PAHs and their separation were computed analytically and used to check the fringe analysis algorithm. The size and separation of the molecules were calculated using the open-source molecule editor and visualisation software Avogadro [27]. The length of each PAH was calculated as the maximum Euclidean distance between two carbon atoms, and the separation between two PAHs as the average separation between adjacent atoms.

4.1.1 Hexabenzocoronene (HBC) stack

The first case selected to test the lattice-fringe program was a stack of HBC molecules (see **Figure 3a**). The stack contains 9 molecules and is taken from a well optimised configuration [17]. **Figures 3a** and **3b** show an image of the stack of HBC molecules and the corresponding simulated TEM. The features identified by the image analysis are shown in **Figures 3c** and **3d**, and are summarised in **Table 3**. The values of the parameters used for the lattice-fringe analysis are presented in **Table 2**. The program is able to map each molecule in the stack. The fringe lengths are in reasonable agreement, with a maximum difference of 17%, but less than 8% in most cases. The inter-layer separation from the image analysis is expected to be larger due to the 'thinning' process where the fringes are reduced to 1-pixel thickness. The results are also in the expected range, with a maximum difference of 23%.

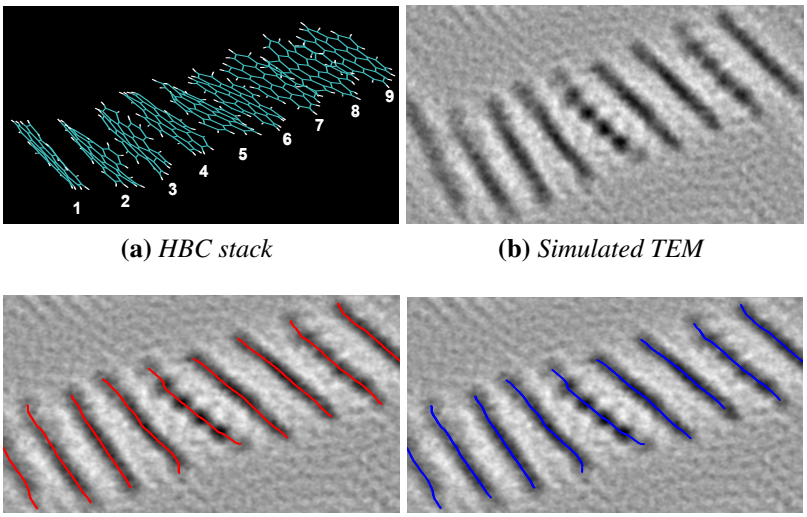

(a) *HBC stack* **(b)** *Simulated TEM*

(c) *Detected fringes* **(d)** *Selected fringes for spacing calculation*

Figure 3: *Simulated TEM: a stack of 9 HBC molecules and corresponding lattice-fringe image analysis.*

4.1.2 Coronene cluster

A cluster of 100 molecules of coronene previously optimised using MD [15] was used to simulate a second TEM image and test the image analysis program (**Figures 4a, 4b**). The features identified by the image analysis are shown in **Figures 4c** and **4d**. The values of the parameters used for the lattice-fringe analysis are presented in **Table 2**.The calculated mean fringe length and separation are presented in **Table 3**. It can be seen from the simulated TEM that the only molecules that appear clearly are those parallel to the beam. In the centre of the cluster it is not possible to discern the molecules. The image code is able to map the coronene molecules parallel to the beam. The calculated sizes and separation are remarkably similar, with slightly larger inter-layer spacing from the image analysis, as expected.

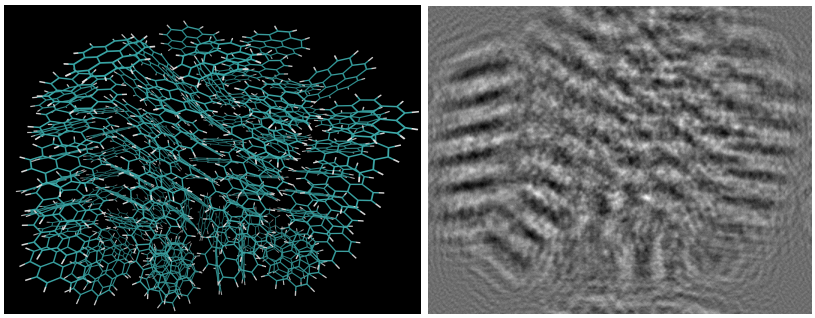

(a) *Coronene Cluster* **(b)** *Simulated TEM (displacement 500)*

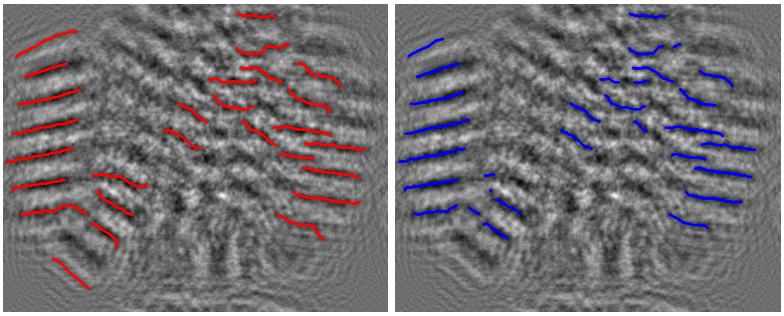

(c) *Detected fringes* **(d)** *Selected fringes for spacing calculation*

Figure 4: *Simulated TEM: a cluster of 100 coronene molecules and corresponding lattice-fringe image analysis.*

Table 3: *HBC stack and Coronene cluster properties measured by the image analysis software.*

Molecule	Fringe length Image analysis (nm)	Fringe length MD simulation (nm)	Inter-layer spacing Image analysis (nm)	Inter-layer spacing MD simulation (nm)
HBC 1	1.066	0.952	0.395	0.375
HBC 2	1.074	1.066	0.458	0.405
HBC 3	1.174	1.113	0.442	0.430
HBC 4	1.25	1.064	0.498	0.465
HBC 5	1.162	1.105	0.479	0.390
HBC 6	1.042	1.056	0.527	0.440
HBC 7	0.989	0.971	0.522	0.420
HBC 8	1.026	1.113	0.470	0.380
HBC 9	0.953	1.099	-	-
Coronene Cluster	0.717[1]	0.730[2]	0.393[1]	0.368[2]

[1] Mean values of detected fringes through image analysis of simulated TEM.
[2] Mean values of measurements from the MD cluster geometry using Avogadro software.

4.2 Evolution of soot in the heptane flame

Soot particles were sampled from the centreline and wings of a 40 mm high non-premixed heptane flame. The sampling locations are defined as per **Figure 1**.

4.2.1 Soot morphology

Low resolution TEM images taken at 15,000× are presented in **Figure 5**. The images were used to measure the size distribution of the primary particles (PP). The distributions were found to be log-normally distributed and are presented in **Figure 6**.

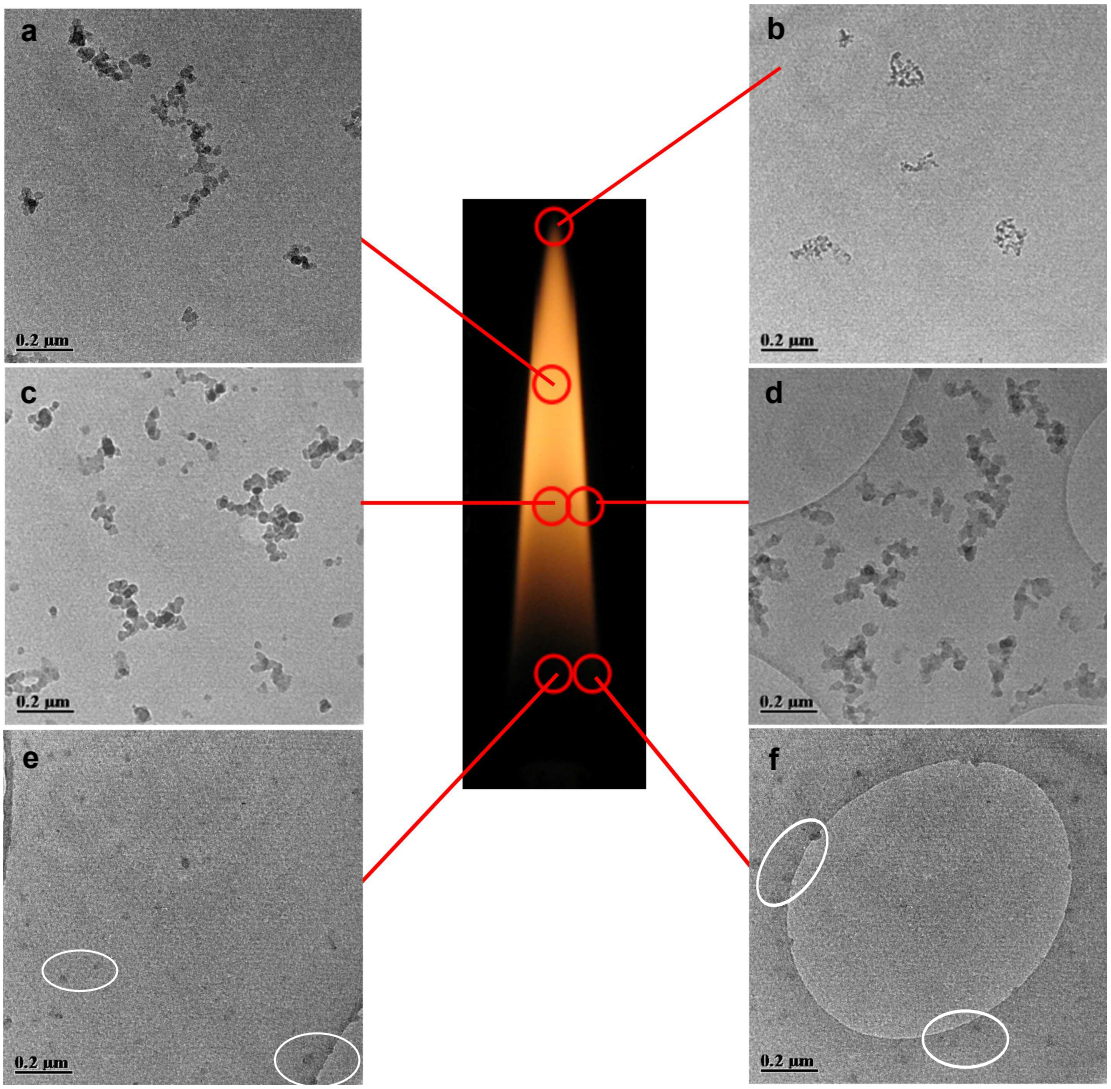

Figure 5: *TEM images of soot in a 40 mm heptane flame (15,000× magnification). Circles in red represent the position where the sample was taken. a) 30 mm HAB, b) 40 mm HAB, c,d) 20 mm HAB and e,f) 10 mm HAB.*

No particles were formed at 5 mm HAB. At 10 mm HAB the TEM images show small

single particles of size 8-18 nm. As we move along the centreline to 20 mm HAB a combination of single particles and large aggregates is observed. At 20 mm HAB in the wings, we also observe a combination of single particles and aggregates, but with a smaller proportion of single particles compared to the centreline. Further downstream, closer to the tip of that flame, mainly aggregates were found with a more dense and compact appearance and less defined boundaries between primary particles. At the tip of the flame, both the aggregates and single particles were observed to have decreased in size.

Nearly spherical particles as small as 6 nm were detected in the inception region of the flame, as pointed by the white circles in **Figures 5 e** and **f**. These single particles grow to sizes as large as 60 nm via surface reactions (including PAH condensation and HACA mechanism) and coalescence of smaller primary particles. Intense aggregation of these particles is observed downstream the flame. In the centre of the flame, large aggregates are seen together with single spherical particles, some of which are small and possibly newly-incepted, and some which have undergone some growth. This bi-modal distribution of particle size has been measured before in similar flames [9–11, 36], and is an indication of persistent particle nucleation throughout the flame followed by coagulation [1].

Looking at the evolution of PP sizes (**Figure 6**), it is observed that the size increases from 10 to 20 mm HAB, but shrinks from 20 to 30 and 40 mm HAB. A rapid reduction in aggregate size is observed close to the tip of the flame, possibly due to particle oxidation as suggested by a previous investigation in the same flame [9].

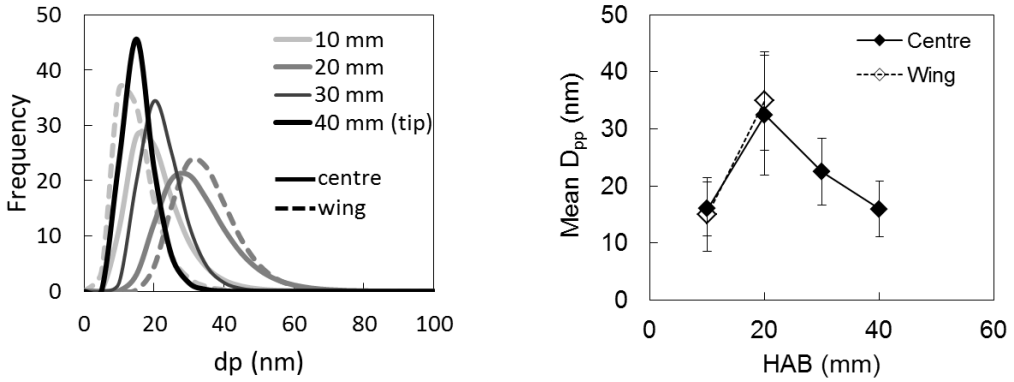

(a) *Log-normal fit of primary particle size distribution. Solid and dashed lines correspond to samples taken in the centerline and the wing respectively.*

(b) *Mean primary particle size at different HABs. The bars correspond to the standard deviation in the mean.*

Figure 6: *Primary particle size of soot particles in a heptane flame of 40 mm. Samples taken along the centerline and in the flame front (wing).*

Some subtle differences were observed in the PP size for samples the taken at the same HAB on the centreline and in the wing of the flame. At 10 mm HAB the PP size on the centerline and in the wing is almost the same. At 20 mm HAB the PP size is slightly larger at the wing. Between the wing and the centerline the PP size is the same at low HAB presumably because newly incepted particles have similar sizes. However, as we move downstream the PP size in the wings is larger, which may be due to the higher

temperature at which soot evolves in the streamlines close to the flame front, promoting greater pyrolysis of the fuel [7, 25]. As the particles approach the tip of the flame, the PP size decreases due to oxidation [9, 11]. The tip region is know to be a highly oxidising environment, where oxygen entrainment and high temperatures promote soot oxidation. Furthermore, measurements reported in similar flames [11] show that the maximum flame temperature is observed somewhere immediately below the tip.

4.2.2 Soot nanostructure

HRTEM images were analysed by lattice-fringe analysis as described in Section 3. **Figure 7** presents some representative high resolution images from the different sampling points. The top row images correspond to soot sampled on the centerline and bottom row to samples on the wings. At a HAB of 10 mm (**Figure 7 a** and **e**), the particles consist of amorphous carbon with very disordered layers, no obvious single centre or concentric shell can be detected. At 20 and 30 mm HAB, soot particles show some degree of graphitisation (**Figure 7 b** and **f**). An 'onion-like' distribution of the fringes is observed, with a disordered core and an outer shell of fringes parallel to the particle perimeter. Nearly spherical PP of different sizes stick to each other can be discerned (this is emphasised in the images with white circles). In **Figure 7d** we see the HRTEM image at the tip of the flame (40 mm HAB). Some organised carbon layers are also observed in smaller 'onion-like' spheres, the PP boundaries become less defined.

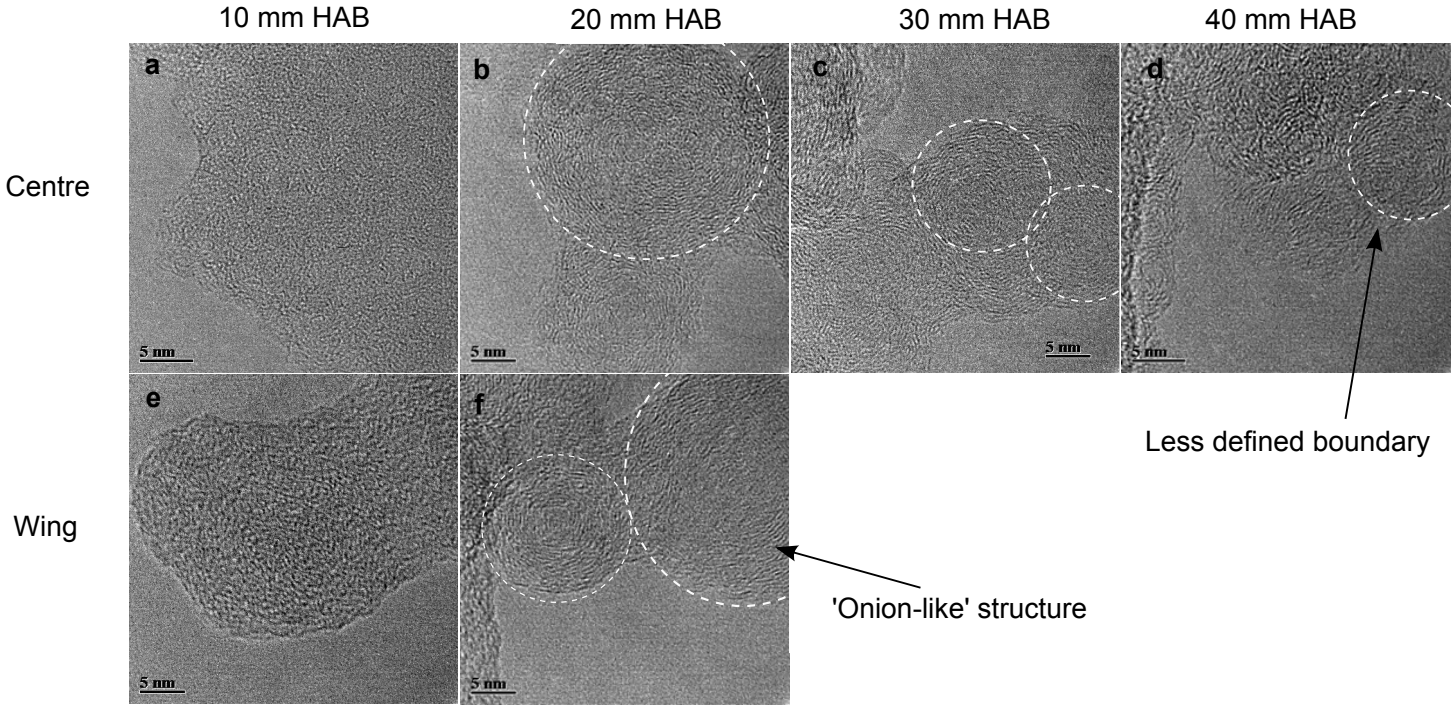

Figure 7: *HRTEM images (at 500,000×) of soot sampled in a 40 mm heptane flame. Top row images correspond to centerline samples; bottom row images were taken in the wing.*

The lattice-fringe analysis provides several statistical metrics describing the nanostruc-

ture. To quantify the extent of graphitisation and obtain possible differences between the samples, we plot the fringe length (FL), tortuosity (FT) and inter-fringe spacing (d) distributions in **Figure 8**.

In principle, all the distributions in **Figure 8** are very close to each other, meaning that there is not substantial differences in the nano-structure of these particles. From the FL distribution (**Figure 8a**) it can be seen that the soot particles at the tip of the flame have the shortest fringes, whereas the largest fringe lengths are found just below the tip at 30 mm HAB. This is further evidence of particle oxidation. In terms of tortuosity and spacing (**Figure 8b and 8c**) the soot samples taken at very low HABs (10 mm) exhibit more tortuous (less straight) and separated fringes, which is expected given that these mostly newly incepted particles that have not yet undergone much graphitisation.

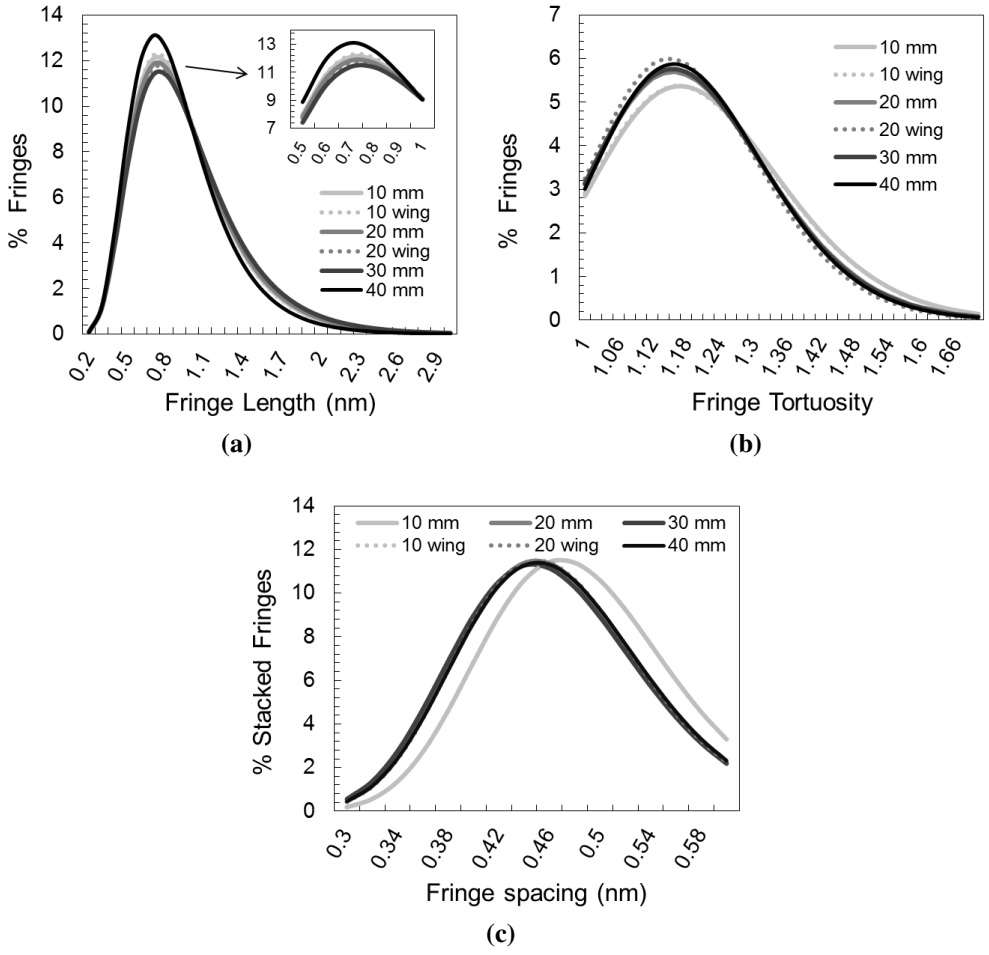

Figure 8: *Log-normal fits to the distributions of a) fringe length, b) fringe tortuosity and c) inter-fringe spacing of soot generated from an heptane flame sampled at different positions. The fits are only meant to guide the eye.*

A summary of the mean lattice-fringe data are presented in **Table 4** with their respective coefficients of variation (ratio of standard deviation σ and the mean value). The table also shows the flame temperature at the each sample point (measured previously,

see [11]). Structural differences between the particles can be obscured by considering only the mean values [6]. To get more information on structural changes the percentage of fringes with high tortuosity (FT > 1.5) and of non-stacked fringes (*nsl*) were also calculated. At low HAB where the smallest particles are detected, the soot presents a very disordered structure with a high tortuosity and *nsl*. This disordered amorphous structure is often used as evidence of PAH coagulation [30, 61], but also the large content of unsaturated hydrocarbons expected in such flame would generate aromatic systems linked with aliphatic bridges that generate more 'chaotic' curved layers [3, 4, 49].

As the particles travel along the flame, a graphitic 'onion like' structure develops where the core remains amorphous and the outer shell graphitises. This is observed between 10 mm and 30 mm HAB, where the mean FL increases and the tortuosity decreases. The inter-layer spacing is reduced, and the number of non-stacked fringes decreases considerably, indicating an increase in the structural order of the soot. The particles size increases through combined surface growth and coalescence [29, 30, 60, 61]. Towards the tip of the flame, oxidation causes a sharp decrease in the FL, but does not significantly affect the other parameters.

Table 4: *Structural parameters of soot by HRTEM and image analysis*

Fuel	HAB (mm)	⟨FL⟩ (nm)	σ/⟨FL⟩ (nm)	⟨FT⟩	σ/⟨FT⟩	%Fringes FT>1.5	⟨d⟩ (nm)	σ/⟨d⟩ (nm)	%nsl	T* (K)
Heptane	10	0.95	0.49	1.205	0.162	7.3	0.477	0.15	57.3	1169
	10 (wing)	0.95	0.49	1.203	0.163	7.6	0.486	0.15	40.1	-
	20	0.96	0.51	1.189	0.155	6.6	0.467	0.16	38.3	1478
	20 (wing)	0.97	0.52	1.180	0.147	5.5	0.468	0.16	38.6	-
	30	0.99	0.51	1.188	0.153	6.2	0.465	0.15	38.5	1694
	40 (tip)	0.91	0.48	1.188	0.147	6.6	0.468	0.16	38.0	1674
H50T50	7	0.98	0.51	1.191	0.153	5.5	0.469	0.16	37.3	1406
	11 (tip)	0.95	0.51	1.184	0.148	6.3	0.469	0.15	39.2	1324
Gasoline	7	0.98	0.52	1.184	0.150	6.0	0.476	0.15	42.3	1313
	11 (tip)	0.97	0.51	1.198	0.160	7.1	0.474	0.15	41.1	1282
Toluene	7 (tip)	0.99	0.50	1.172	0.164	5.0	0.449	0.16	35.8	1239

*Temperature values taken from [11]

4.3 Comparison of soot from the heptane, H50T50, gasoline and toluene flames

4.3.1 Soot morphology

Representative TEM images of soot sampled from the tips of the heptane, H50T50, gasoline and toluene flames are presented in **Figure 9**. The left column contains low-magnification images (40,000×), it can be observed that the aggregate and PP sizes in the H50T50 flame are larger than in the heptane flame, whilst the largest particles are formed in the toluene

flame. Similar behaviour was seen in a previous study of similar flames, where the aggregate sizes were measured using mobility spectroscopy [11].

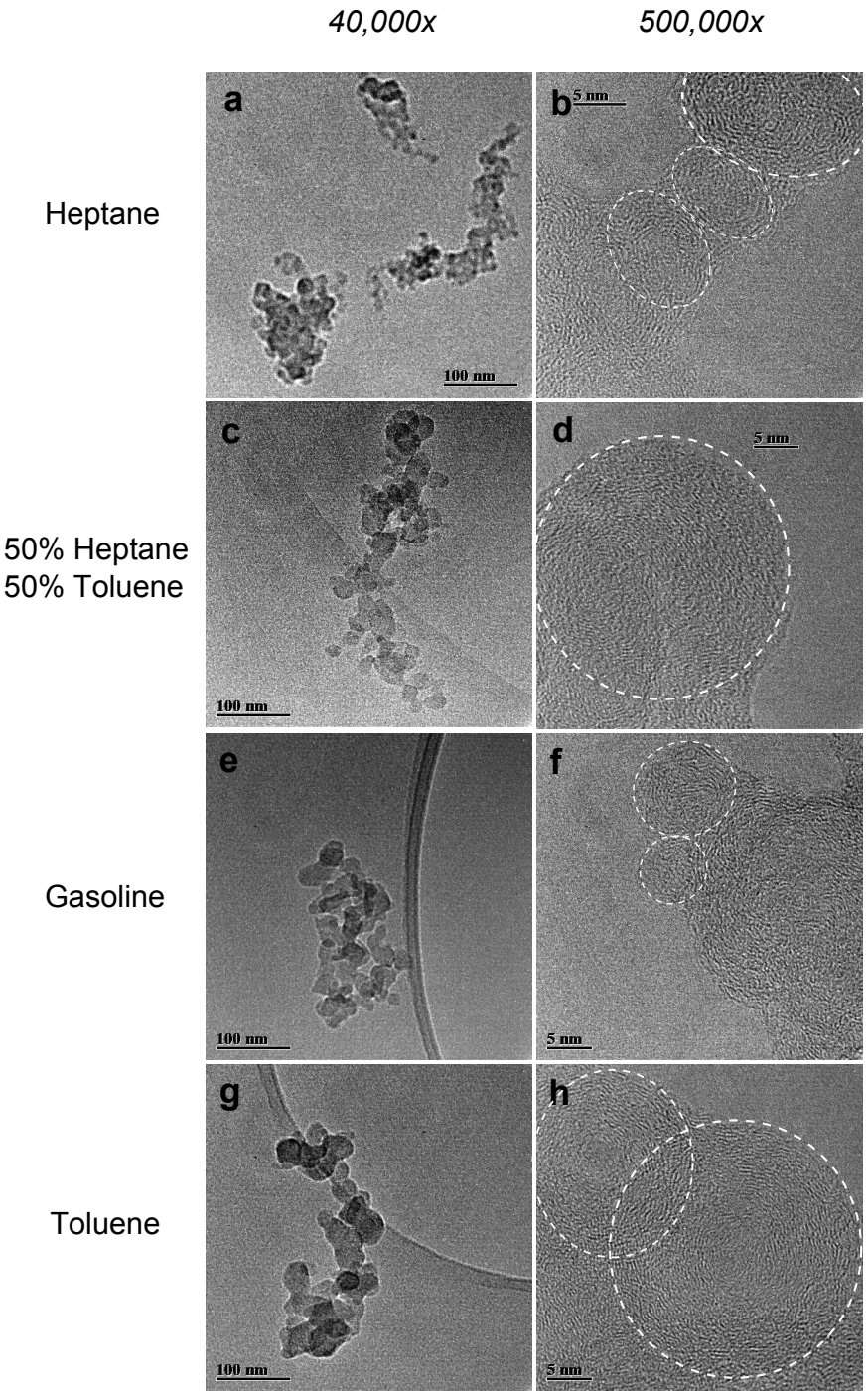

Figure 9: *HRTEM of soot particles sampled at the tip of the flame from different fuels. The left column shows TEM images at 40,000× magnification. The right column shows HRTEM images at 500,000× magnification. a and b) Heptane 40 mm HAB, c and d) H50T50 11 mm HAB, e and f) Gasoline 11 mm HAB, g and h) Toluene 7 mm HAB.*

The particle size distributions and the mean PP size are presented in **Figure 10**. It is clear that the PP size decreases when reaching the tip of the flame, although the difference is less distinct in the H50T50 flame. The PP size increases with the aromaticity of the fuel, where the aromatic content of the fuels is in the order heptane < gasoline < H50T50 < toluene. Considering that the comparison is made for samples at or close to the tip of the flame, oxidation should also play an important role.

The maximum temperature in the heptane flame is 1770 K on the centreline compared to 1674 K at the tip, whereas the other fuels exhibit similar maximum temperatures between 1410 K - 1460 K (considering an error of ∼40 K) and even lower at the tip. This large difference in temperature translates into a stronger oxidising environment in the heptane flame. It can be seen in **Figures 10b and 6b** that the maximum mean PP size attained in the heptane flame (at 20 mm HAB) is comparable to that in the toluene flame.

The effect of aromatic content is observed beyond its impact on the flame temperature and therefore the rate of oxidation. The flames of toluene, H50T50 and gasoline exhibited similar and relatively low flame temperatures where oxidation would not be as strong. However, the size increases with the aromaticity of the fuel due to a larger abundance of intact aromatic radical species and relatively poor unsaturated light hydrocarbons[11, 19, 64]. Although the H50T50 mixture and gasoline have the same smoke point and similar flame temperatures, the PP and aggregates (as measured previously [11]) are smaller in the gasoline flame. This is attributed to the molecular structure of the aromatic species in the gasoline fuel.

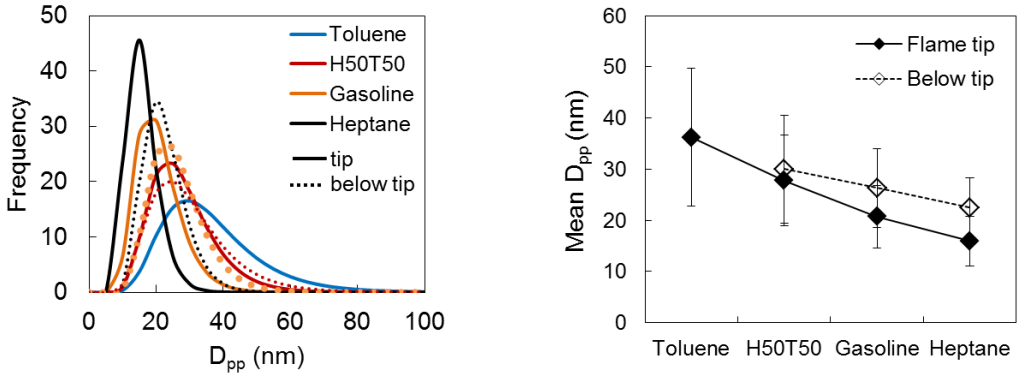

(a) *Log-normal fit of primary particle size distribution. Solid lines and dashed lines correspond to samples taken at the tip and below the tip of the flame respectively.*

(b) *Mean primary particle size for at and below the tip of the flames. The bars correspond to the standard deviation of the mean.*

Figure 10: *Primary particle size of soot sampled in heptane, H50T50, gasoline and toluene flames. Samples are taken below and at the tip of the flame.*

4.3.2 Soot nanostructure

Representative HRTEM images are shown in the right column of **Figure 9**. Soot particles from all the fuels exhibit the 'onion-like' fringe arrangement. The differences in PP size

observed at low resolution are also seen here with the size of the 'onions'. Qualitatively, at the tip, soot from the heptane flame seems to have shorter and more curved fringes compared to H50T50 and gasoline, indicating a lesser degree of graphitisation. Soot particles from toluene seem to be the most graphitic, with a larger concentric shell of parallel fringes and smaller disordered core.

The fringe parameter distributions from the samples taken at the tip of the flame are presented in **Figure 11**. The mean values of parameters are summarised in **Table 4** for all the samples. Toluene flame presents the most ordered and graphitised soot particles, larger fringes with the smallest FT (and highly tortuous fringes), significantly smaller d and the largest number of stacked fringes. Russo et al. [49] suggested that he abundance of aromatic radicals promotes rapid PAH growth and the lack of unsaturated hydrocarbons limits the amount of disorder imposed via aliphatic cross linking.

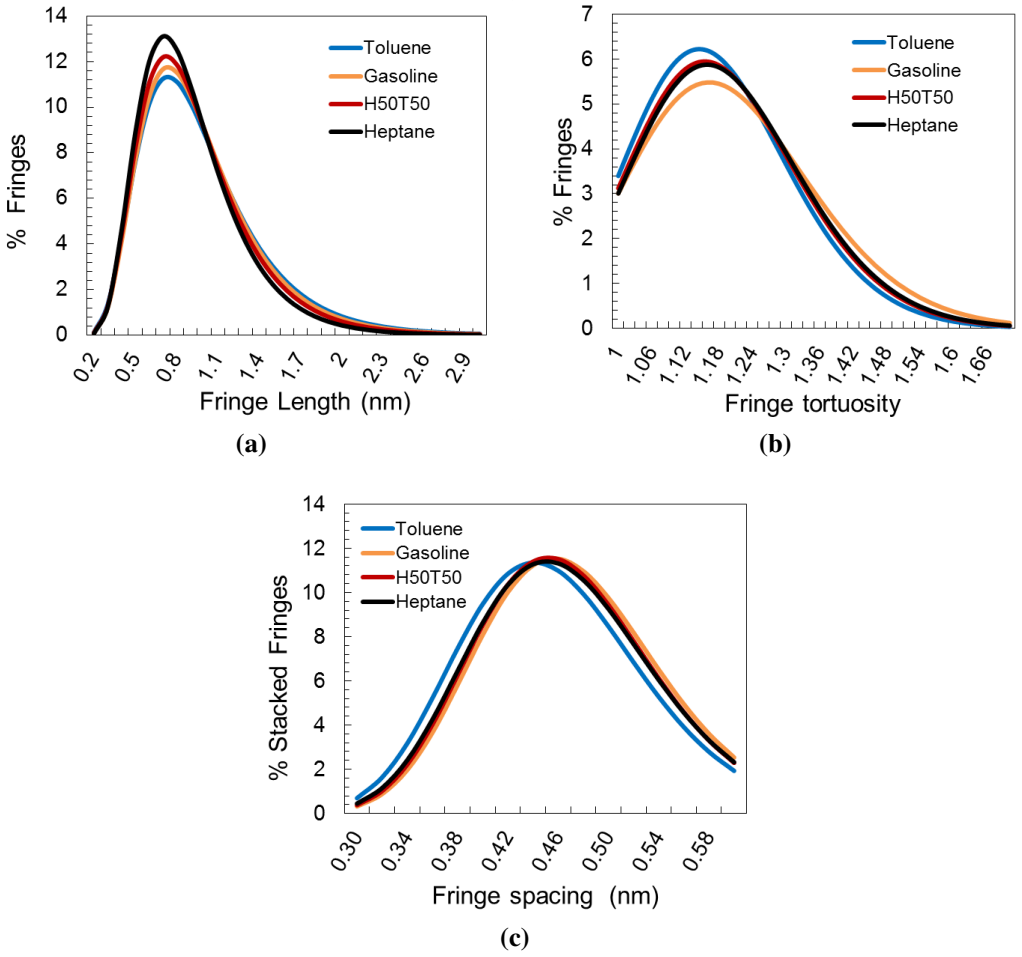

Figure 11: *Log-normal fits to the distributions of a) fringe length, b) fringe tortuosity and c) inter-fringe spacing of soot generated at the tip of flames of toluene, H50T50, gasoline and heptane. The fits are only meant to guide the eye.*

The soot samples taken at the tip of the flames show higher values of the FL, FT, highly tortuous fringes, d and nsl for gasoline compared to H50T50 and heptane, suggesting

larger but more disordered carbon layers. Soot images below the tip (7 mm HAB) and at the tip (11 mm HAB) of H50T50 and gasoline flames are shown in **Figure 12**. From the image analysis (**Table4**), it can be seen that the FL of H50T50 soot decreases sharply compared to the gasoline flame. Also, the number of highly tortuous fringes increases for both fuels once particles reach the tip of the flame.

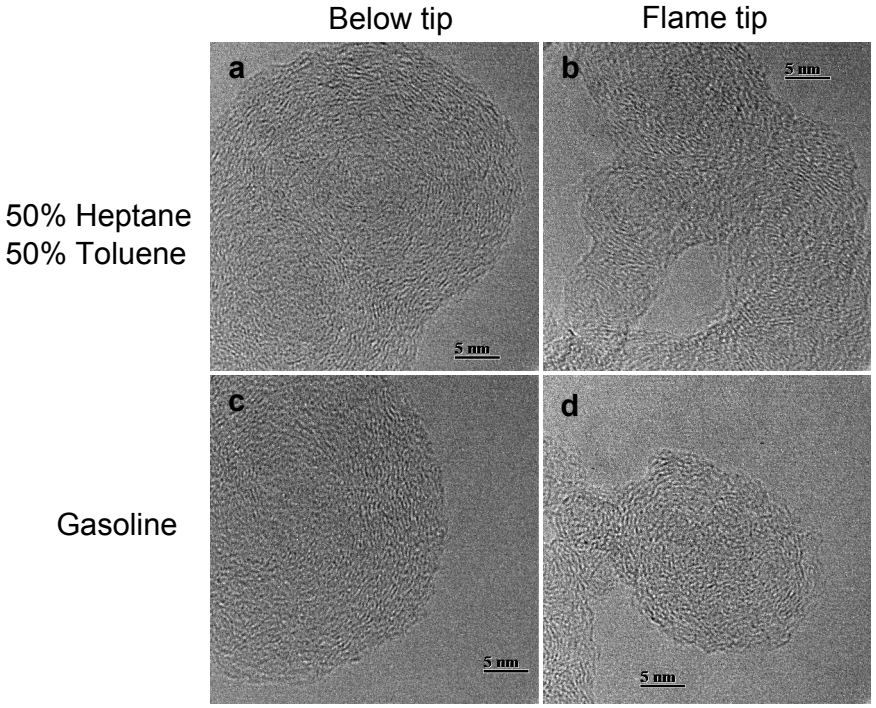

Figure 12: *HRTEM of soot particles at 500,000× magnification. a) H50T50 7 mm HAB, b) H50T50 11 mm HAB (tip), c) Gasoline 7 mm HAB and d) Gasoline 11 mm HAB (tip).*

The soot in the heptane flame develop a similar degree of order compared to the soot in the aromatic flames. As shown in **Table 4**, the FL, FT, *d* and *nsl* in the heptane flame at 20 and 30 mm HABs are similar to those of the H50T50, gasoline and even toluene. However, as the particles approach the tip of the heptane flame, the stronger oxidising environment causes a much greater reduction in the graphitic order of the particles in the heptane flame (see **Figures 7** and **8** and **Table 4**). Although the heptane flame probably does not contain as many aromatic radicals for PAH growth as the flames of the other fuels, in the soot formation region the high temperature conditions and the higher concentration of hydrogen, acetylene and diacetylene can favour the HACA mechanism as observed by Alfe et al. [5], suggesting C_2H_2 as the dominant growth species. Furthermore, at higher temperatures, Chen et al. [16] found that more surface sites may be activated compared to other environments where low temperatures may cause many potential sites to be inactive.

The mean fringe length of 0.95-0.99 nm observed in all flames corresponds to the size of four aromatic rings. Assuming that the PAHs in the soot particles have parallelogram shape [6, 22, 37] or D_{2h}-symmetry [2] we estimate PAHs with 14-16 aromatic rings, the size of cirumpyrene.

5 Conclusions

An image analysis code was developed to quantify the nanostructure of soot particles imaged via HRTEM. The code was tested using simulated TEM images of clusters of molecules with known geometries. The lattice-fringe code is able to map the molecules in the simulated TEM images. It accurately measures the size of the molecules, but because of the method of analysis and similar to other codes, it systematically over estimates the inter-layer spacing between the molecules.

The nanostrucutre and evolution of soot particles was investigated using HRTEM and lattice-fringe analysis along the centre line and in the wings of liquid-fuelled non-premixed wick-fed laminar diffusion flames. The fuels considered were heptane, a commercial gasoline, an iso-volumetric heptane-toluene mixture and pure toluene.

Single primary particles as small as 6 nm were detected in the inception region of the flames. The particles grew to sizes as large as 60 nm, eventually forming large aggregates composed of many primary. The evolution of the soot nanostructure showed evidence of PAH coagulation in the inception region. As the particles travel through the flame, a graphitic order develops where the core remains amorphous and the outer shell graphitises. At the tip of the flame, oxidation causes a sharp decrease in the fringe length, but does not significantly affects the tortuosity and inter-fringe spacing. Particle oxidation was observed at the tip of all flames.

Temperature and fuel type were found to have a significant influence on the nanostrucutre of the soot particles. The aromaticity of the fuel translates into larger primary particles with increased structural order. Toluene exhibits the largest degree of graphitisation, with large fringe lengths, many stacked fringes and low tortuosity and inter-layer spacing. Heptane develops a similar degree of order as the aromatic flames, in terms of fringe length, tortuosity, spacing and stacking. However, it presents stronger soot oxidation (due to higher temperature) at the tip that reduces the fringe lengths and increases the highly tortuous fringes.

The mean fringe lengths estimated from all the fuels and sample points in the flames correspond to PAHs with an average size of 14-16 aromatic rings. The main differences in the nanostructure of the soot was the arrangement and degree of order of the PAHs within each particle.

6 Acknowledgments

M.B acknowledges financial support provided by the Administrative Department of Science, Technology and Innovation of Colombia. This project is partly funded by the National Research Foundation (NRF), Prime Minister's Office, Singapore under its Campus for Research Excellence and Technological Enterprise (CREATE) programme.

References

[1] A. Abid, N. Heinz, E. Tolmachoff, D. Phares, C. Campbell, and H. Wang. On evolution of particle size distribution functions of incipient soot in premixed ethylene-oxygen-argon flames. *Combustion and Flame*, 154:775–788, 2008.

[2] E. M. Adkins and J. H. Miller. Extinction measurements for optical band gap determination of soot in a series of nitrogen-diluted ethylene/air non-premixed flames. *Physical Chemistry Chemical Physics*, 17:2686–2695, 2015. doi:10.1039/C4CP04452E.

[3] M. Alfe, B. Apicella, R. Barbella, A. Tregrossi, and A. Ciajolo. Similarities and dissimilarities in n-hexane and benzene sooting premixed flames. *Proceedings of the Combustion Institute*, 31(1):585 – 591, 2007. ISSN 1540-7489. doi:10.1016/j.proci.2006.07.187.

[4] M. Alfe, B. Apicella, R. Barbella, J.-N. Rouzaud, A. Tregrossi, and A. Ciajolo. Structure-property relationship in nanostructures of young and mature soot in premixed flames. *Proceedings of the Combustion Institute*, 32(1):697 – 704, 2009. ISSN 1540-7489. doi:10.1016/j.proci.2008.06.193.

[5] M. Alfe, B. Apicella, J.-N. Rouzaud, A. Tregrossi, and A. Ciajolo. The effect of temperature on soot properties in premixed methane flames. *Combustion and Flame*, 157(10):1959 – 1965, 2010. ISSN 0010-2180. doi:10.1016/j.combustflame.2010.02.007.

[6] B. Apicella, P. Pre, M. Alfe, A. Ciajolo, V. Gargiulo, C. Russo, A. Tregrossi, D. Deldique, and J. Rouzaud. Soot nanostructure evolution in premixed flames by high resolution electron transmission microscopy (HRTEM). *Proceedings of the Combustion Institute*, 35(2):1895 – 1902, 2015. ISSN 1540-7489. doi:10.1016/j.proci.2014.06.121.

[7] J. Appel, H. Bockhorn, and M. Frenklach. Kinetic modeling of soot formation with detailed chemistry and physics: laminar premixed flames of C2 hydrocarbons. *Combustion and Flame*, 121(1-2):122 – 136, 2000. ISSN 0010-2180. doi:10.1016/S0010-2180(99)00135-2.

[8] ASTM. Standard test method for smoke point of kerosine and aviation turbine fuel. *ASTM Standard D1322-08*, 1997.

[9] M. L. Botero, S. Mosbach, and M. Kraft. Sooting tendency of paraffin components of diesel and gasoline in diffusion flames. *Fuel*, 126:8 – 15, 2014. ISSN 0016-2361. doi:10.1016/j.fuel.2014.02.005.

[10] M. L. Botero, S. Mosbach, J. Akroyd, and M. Kraft. Sooting tendency of surrogates for the aromatic fractions of diesel and gasoline in a wick-fed diffusion flame. *Fuel*, 153:31 – 39, 2015. ISSN 0016-2361. doi:10.1016/j.fuel.2015.02.108.

[11] M. L. Botero, S. Mosbach, and M. Kraft. Sooting tendency and particle size distributions of n-heptane/toluene mixtures burned in a wick-fed diffusion flame. Submitted for publication, 2015.

[12] H. F. Calcote and D. M. Manos. Effect of molecular structure on incipient soot formation. *Combustion and Flame*, 49(1 - 3):289–304, 1983. doi:10.1016/0010-2180(83)90172-4.

[13] D. Chen, Z. Zainuddin, E. Yapp, J. Akroyd, S. Mosbach, and M. Kraft. A fully coupled simulation of PAH and soot growth with a population balance model. *Proceedings of the Combustion Institute*, 34(1):1827 – 1835, 2013. ISSN 1540-7489. doi:10.1016/j.proci.2012.06.089.

[14] D. Chen, T. S. Totton, J. Akroyd, S. Mosbach, and M. Kraft. Phase change of polycyclic aromatic hydrocarbon clusters by mass addition. *Carbon*, 77(0):25 – 35, 2014. ISSN 0008-6223. doi:10.1016/j.carbon.2014.04.089.

[15] D. Chen, T. S. Totton, J. Akroyd, S. Mosbach, and M. Kraft. Size-dependent melting of polycyclic aromatic hydrocarbon nano-clusters: A molecular dynamics study. *Carbon*, 67(0):79 – 91, 2014. ISSN 0008-6223. doi:10.1016/j.carbon.2013.09.058.

[16] D. Chen, J. Akroyd, S. Mosbach, and M. Kraft. Surface reactivity of polycyclic aromatic hydrocarbon clusters. *Proceedings of the Combustion Institute*, 35(2):1811 – 1818, 2015. ISSN 1540-7489. doi:10.1016/j.proci.2014.06.140.

[17] D. Chen, J. Akroyd, S. Mosbach, D. Opalka, and M. Kraft. Solid-liquid transitions in homogenous ovalene, hexabenzocoronene and circumcoronene clusters: A molecular dynamics study. *Combustion and Flame*, 162(2):486 – 495, 2015. ISSN 0010-2180. doi:10.1016/j.combustflame.2014.07.025.

[18] H. Chen and R. Dobbins. Crystallogenesis of particles formed in hydrocarbon combustion. *Combustion Science and Technology*, 159(1):109–128, 2000. doi:10.1080/00102200008935779.

[19] A. D'Anna, A. Ciajolo, M. Alfè, B. Apicella, and A. Tregrossi. Effect of fuel/air ratio and aromaticity on the molecular weight distribution of soot in premixed n-heptane flames. *Proceedings of the Combustion Institute*, 32(1):803 – 810, 2009. ISSN 1540-7489. doi:10.1016/j.proci.2008.06.198.

[20] R. A. Dobbins and C. M. Megaridis. Morphology of flame-generated soot as determined by thermophoretic sampling. *Langmuir*, 3(2):254–259, 1987. doi:10.1021/la00074a019.

[21] F. Douce, N. Djebaïli-Chaumeix, C.-E. Paillard, C. Clinard, and J.-N. Rouzaud. Soot formation from heavy hydrocarbons behind reflected shock waves. *Proceedings of the Combustion Institute*, 28(2):2523 – 2529, 2000. ISSN 1540-7489. doi:10.1016/S0082-0784(00)80668-2.

[22] V. Fernandez-Alos, J. K. Watson, R. VanderWal, and J. P. Mathews. Soot and char molecular representations generated directly from HRTEM lattice fringe images using Fringe3D. *Combustion and Flame*, 158(9):1807 – 1813, 2011. ISSN 0010-2180. doi:10.1016/j.combustflame.2011.01.003.

[23] M. Frenklach and H. Wang. *Soot Formation in Combustion - Mechanisms and Models*. Springer-Verlag, 1994.

[24] I. Glassman. Soot formation in combustion processes. *Symposium (International) on Combustion*, 22(1):295 – 311, 1989. ISSN 0082-0784. doi:10.1016/S0082-0784(89)80036-0.

[25] A. Gomez, M. G. Littman, and I. Glassman. Comparative study of soot formation on the centreline of axisymmetric laminar diffusion flames: Fuel and temperature effects. *Combustion and Flame*, 70:225–241, 1987.

[26] W.-Q. Han, L. Wu, Y. Zhu, K. Watanabe, and T. Taniguchi. Structure of chemically derived mono- and few-atomic-layer boron nitride sheets. *Applied Physics Letters*, 93(22):223103, 2008. doi:10.1063/1.3041639.

[27] M. D. Hanwell, D. E. Curtis, D. C. Lonie, T. Vandermeersch, E. Zurek, and G. R. Hutchison. Avogadro: An advanced semantic chemical editor, visualization, and analysis platform. *Journal of Cheminformatics*, 1:4 – 17, 2012. doi:10.1186/1758-2946-4-17.

[28] P. J. F. Harris and S. C. Tsang. High-resolution electron microscopy studies of non-graphitizing carbons. *Philosophical Magazine A*, 76(3):667–677, 1997. doi:10.1080/01418619708214028.

[29] K. Hayashida, T. Mogi, K. Amagai, and M. Arai. Growth characteristics of polycyclic aromatic hydrocarbons in dimethyl ether diffusion flame. *Fuel*, 90(2):493 – 498, 2011. ISSN 0016-2361. doi:10.1016/j.fuel.2010.10.012.

[30] K. Hayashida, S. Nagaoka, and H. Ishitani. Growth and oxidation of graphitic crystallites in soot particles within a laminar diffusion flame. *Fuel*, 128(0):148 – 154, 2014. ISSN 0016-2361. doi:10.1016/j.fuel.2014.03.008.

[31] T. Ishiguro, Y. Takatori, and K. Akihama. Microstructure of diesel soot particles probed by electron microscopy: First observation of inner core and outer shell. *Combustion and Flame*, 108(1-2):231 – 234, 1997. ISSN 0010-2180. doi:10.1016/S0010-2180(96)00206-4.

[32] H. Jung, D. B. Kittelson, and M. R. Zachariah. Kinetics and visualization of soot oxidation using transmission electron microscopy. *Combustion and Flame*, 136(4): 445 – 456, 2004. ISSN 0010-2180. doi:10.1016/j.combustflame.2003.10.013.

[33] E. J. Kirkland. *Advanced Computing in Electron Microscopy*. Plenum Publishing, New York, 1998. ISBN 0-306-45936-1.

[34] S. Kook and L. M. Pickett. Soot volume fraction and morphology of conventional and surrogate jet fuel sprays at 1000 K and 6.7 MPa ambient conditions. *Proceedings of the Combustion Institute*, 33(2):2911 – 2918, 2011. ISSN 1540-7489. doi:10.1016/j.proci.2010.05.073.

[35] S. Kook and L. M. Pickett. Soot volume fraction and morphology of conventional fischer-tropsch, coal-derived, and surrogate fuel at diesel conditions. *SAE technical paper*, (2012-01-0678), 2012. doi:10.4271/2012-01-0678.

[36] M. Maricq. Soot formation in ethanol/gasoline fuel blend diffusion flames. *Combustion and Flame*, 159(1):170 – 180, 2012. ISSN 0010-2180. doi:10.1016/j.combustflame.2011.07.010.

[37] J. P. Mathews, V. Fernandez-Also, A. D. Jones, and H. H. Schobert. Determining the molecular weight distribution of pocahontas no. 3 low-volatile bituminous coal utilizing HRTEM and laser desorption ionization mass spectra data. *Fuel*, 89(7):1461 – 1469, 2010. ISSN 0016-2361. doi:10.1016/j.fuel.2009.10.014. 17th International Symposium on Alcohol Fuels.

[38] O. Mathieu, N. Djebaïli-Chaumeix, C.-E. Paillard, and F. Douce. Experimental study of soot formation from a diesel fuel surrogate in a shock tube. *Combustion and Flame*, 156(8):1576 – 1586, 2009. ISSN 0010-2180. doi:10.1016/j.combustflame.2009.05.002.

[39] MATLAB. *version 8.2.0.701 (R2013b)*. The MathWorks Inc., Natick, Massachusetts, 2013.

[40] C. S. McEnally, L. D. Pfefferle, B. Atakan, and K. Kohse-Höinghaus. Studies of aromatic hydrocarbon formation mechanisms in flames: Progress towards closing the fuel gap. *Progress in Energy and Combustion Science*, 32(3):247–294, 2006. ISSN 0360-1285. doi:10.1016/j.pecs.2005.11.003.

[41] J. C. Meyer, C. Kisielowski, R. Erni, M. D. Rossell, M. F. Crommie, and A. Zettl. Direct imaging of lattice atoms and topological defects in graphene membranes. *Nano Letters*, 8(11):3582–3586, 2008. doi:10.1021/nl801386m.

[42] J. C. Meyer, S. Kurasch, H. J. Park, V. Skakalova, D. Kunzel, A. Gross, A. Chuvilin, G. Algara-Siller, S. Roth, T. Iwasaki, U. Starke, J. H. Smet, and U. Kaiser. Experimental analysis of charge redistribution due to chemical bonding by high-resolution transmission electron microscopy. *Nature Materials*, 10(3):209–215, 2011. doi:10.1038/nmat2941.

[43] J. H. Miller, J. D. Herdman, C. D. Green, and E. M. Webster. Experimental and computational determinations of optical band gaps for PAH and soot in a N2-diluted, ethylene/air non-premixed flame. *Proceedings of the Combustion Institute*, 34(2): 3669 – 3675, 2013. ISSN 1540-7489. doi:10.1016/j.proci.2012.05.054.

[44] A. Onischuk, S. diStasio, V. Karasev, A. Baklanov, G. Makhov, A. Vlasenko, A. Sadykova, A. Shipovalov, and V. Panfilov. Evolution of structure and charge of soot aggregates during and after formation in a propane/air diffusion flame. *Journal*

of Aerosol Science, 34(4):383 – 403, 2003. ISSN 0021-8502. doi:10.1016/S0021-8502(02)00215-X.

[45] A. Palotas, L. Rainey, C. Feldermann, A. Sarofim, and J. V. Sande. Soot morphology: An application of image analysis in high-resolution transmission electron microscopy. *Microscopy Research Technology*, 33(3):266–278, 1996.

[46] P. Pre, G. Huchet, D. Jeulin, J.-N. Rouzaud, M. Sennour, and A. Thorel. A new approach to characterize the nanostructure of activated carbons from mathematical morphology applied to high resolution transmission electron microscopy images. *Carbon*, 52(0):239 – 258, 2013. ISSN 0008-6223. doi:10.1016/j.carbon.2012.09.026.

[47] H. Richter and J. Howard. Formation of polycyclic aromatic hydrocarbons and their growth to soot - a review of chemical reaction pathways. *Progress in Energy and Combustion Science*, 26(4 - 6):565 – 608, 2000. ISSN 0360-1285. doi:10.1016/S0360-1285(00)00009-5.

[48] J.-N. Rouzaud and C. Clinard. Quantitative high-resolution transmission electron microscopy: A promising tool for carbon materials characterization. *Fuel Processing Technology*, 77-78(0):229 – 235, 2002. ISSN 0378-3820. doi:10.1016/S0378-3820(02)00053-X.

[49] C. Russo, M. Alfe, J.-N. Rouzaud, F. Stanzione, A. Tregrossi, and A. Ciajolo. Probing structures of soot formed in premixed flames of methane, ethylene and benzene. *Proceedings of the Combustion Institute*, 34(1):1885 – 1892, 2013. ISSN 1540-7489. doi:10.1016/j.proci.2012.06.127.

[50] M. Sander, R. I. Patterson, A. Braumann, A. Raj, and M. Kraft. Developing the PAH-PP soot particle model using process informatics and uncertainty propagation. *Proceedings of the Combustion Institute*, 33(1):675 – 683, 2011. ISSN 1540-7489. doi:10.1016/j.proci.2010.06.156.

[51] C.-C. Scott, M. C.and Chen, M. Mecklenburg, C. Zhu, R. Xu, P. Ercius, U. Dahmen, B. C. Regan, and J. Miao. Electron tomography at 2.4-angstrom resolution. *Nature*, 483(7390):444–447, 2011. doi:10.1038/nature10934.

[52] A. Sharma, T. Kyotani, and A. Tomita. A new quantitative approach for microstructural analysis of coal char using HRTEM images. *Fuel*, 78(10):1203 – 1212, 1999. ISSN 0016-2361. doi:10.1016/S0016-2361(99)00046-0.

[53] H.-S. Shim, R. H. Hurt, and N. Y. Yang. A methodology for analysis of 002 lattice fringe images and its application to combustion-derived carbons. *Carbon*, 38(1):29 – 45, 2000. ISSN 0008-6223. doi:10.1016/S0008-6223(99)00096-2.

[54] K. Siegmann, K. Sattler, and H. Siegmann. Clustering at high temperatures: carbon formation in combustion. *Journal of Electron Spectroscopy and Related Phenomena*, 126(1-3):191 – 202, 2002. ISSN 0368-2048. doi:10.1016/S0368-2048(02)00152-4.

[55] P. Toth, A. Palotas, J. Lighty, and C. Echavarria. Quantitative differentiation of poorly ordered soot nanostructures: A semi-empirical approach. *Fuel*, 99(0):1 – 8, 2012. ISSN 0016-2361. doi:10.1016/j.fuel.2012.04.013.

[56] T. S. Totton, D. Chakrabarti, A. J. Misquitta, M. Sander, D. J. Wales, and M. Kraft. Modelling the internal structure of nascent soot particles. *Combustion and Flame*, 157(5):909 – 914, 2010. ISSN 0010-2180. doi:10.1016/j.combustflame.2009.11.013.

[57] R. VanderWal. A TEM methodology for the study of soot particle structure. *Combustion Science and Technology*, 126(1-6):333–351, 1997. doi:10.1080/00102209708935680.

[58] R. VanderWal and A. J. Tomasek. Soot nanostructure: dependence upon synthesis conditions. *Combustion and Flame*, 136(1-2):129 – 140, 2004. ISSN 0010-2180. doi:10.1016/j.combustflame.2003.09.008.

[59] R. VanderWal, A. J. Tomasek, and J. D. King. A method for structural characterization of the range of cylindrical nanocarbons: Nanotubes to nanofibers. *Carbon*, 43 (14):2918 – 2930, 2005. ISSN 0008-6223. doi:10.1016/j.carbon.2005.06.026.

[60] R. VanderWal, V. M. Bryg, and M. D. Hays. Fingerprinting soot (towards source identification): Physical structure and chemical composition. *Journal of Aerosol Science*, 41(1):108 – 117, 2010. ISSN 0021-8502. doi:10.1016/j.jaerosci.2009.08.008. Special Issue for the 9th International Conference on Carbonaceous Particles in the Atmosphere.

[61] R. VanderWal, V. M. Bryg, and C.-H. Huang. Aircraft engine particulate matter: Macro- micro- and nanostructure by HRTEM and chemistry by XPS. *Combustion and Flame*, 161(2):602 – 611, 2014. ISSN 0010-2180. doi:10.1016/j.combustflame.2013.09.003.

[62] H. Wang. Formation of nascent soot and other condensed-phase materials in flames. *Proceedings of the Combustion Institute*, 33(1):41 – 67, 2011. ISSN 1540-7489. doi:10.1016/j.proci.2010.09.009.

[63] R. J. Watson, M. L. Botero, C. J. Ness, N. M. Morgan, and M. Kraft. An improved methodology for determining threshold sooting indices from smoke point lamps. *Fuel*, 111:120 – 130, 2013. ISSN 0016-2361. doi:10.1016/j.fuel.2013.04.024.

[64] J. Wei, C. Song, G. Lv, J. Song, L. Wang, and H. Pang. A comparative study of the physical properties of in-cylinder soot generated from the combustion of n-heptane and toluene/n-heptane in a diesel engine. *Proceedings of the Combustion Institute*, 35(2):1939 – 1946, 2015. ISSN 1540-7489. doi:10.1016/j.proci.2014.06.011.

[65] K. Yehliu, R. VanderWal, and A. L. Boehman. Development of an HRTEM image analysis method to quantify carbon nanostructure. *Combustion and Flame*, 158(9): 1837 – 1851, 2011. ISSN 0010-2180. doi:10.1016/j.combustflame.2011.01.009.

A Lattice-fringe algorithm

The algorithm developed for the analysis of HRTEM images is represented in **Figure 13**. An example of the steps taken for image manipulation is shown in **Figure 14**. Each step is described in detail below.

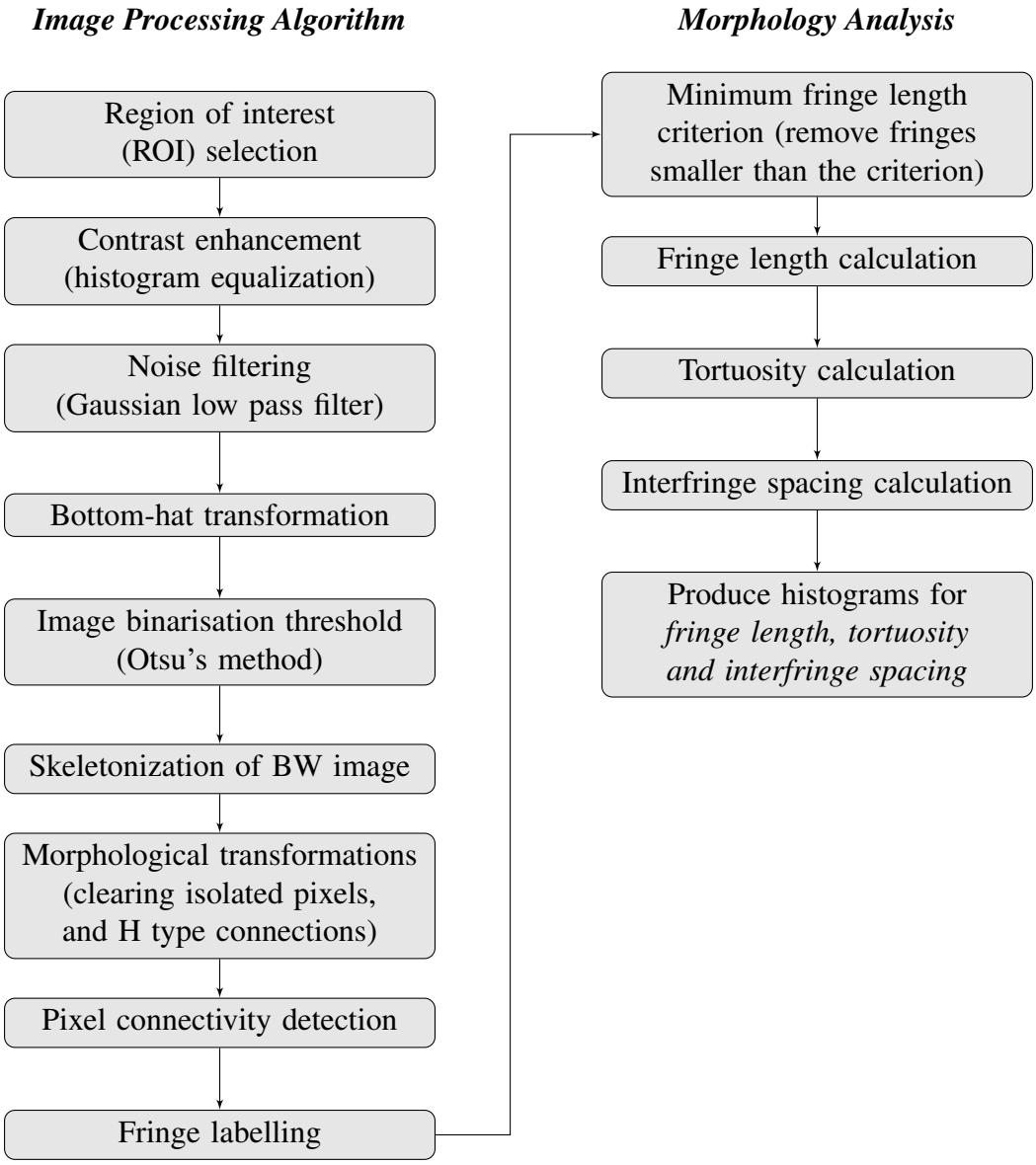

Figure 13: *Flow chart of the main processing steps of the HRTEM image analysis*

Region of interest (ROI)

Select a region of the image that provides clearer information of the fringes. All the pixels outside the ROI are forced to take intensity values of 0 as shown in **Figure 14b**.

Contrast enhancement

Histogram equalisation is used to enhance the image contrast. The intensity histogram of

the image is transformed into a uniform probability density function. This function tends to introduce noise in the background. **Figure 14c**.

Gaussian lowpass filter

High frequencies are eliminated using a low pass filter. A Gaussian mask is applied to smooth the the edges between the image and frequency filters, as depicted in **Figure 14d**.

Binarisation

A bottom-hat transformation is used to highlight darker spots on the original image. The image is first dilated with a structuring element, then eroded by the same element. This process is used to correct uneven illumination, and to remove very small dark features (those smaller than the structuring element) (see **Figure 14e**). The binary image is finally converted to a greyscale using Otsu's method. The result is shown in **Figure 14f**.

Skeletonization

An iterative thinning is used to remove the boundaries pixels of the object until the residual object has 1-pixel thickness, at which point no further change is observed. **Figure 14g** illustrates the skeletonisation process.

Additional morphological operation

Some additional operations can be performed to improve the final image before the fringes are labelled. For example, clearing single isolated pixels, or breaking fringes in "H" form.

Fringe length analysis

Once the skeleton of the binary image is complete, the connectivity of all pixels is obtained. All pixels with more than three connections (branched fringes), were eliminated. The remaining connected pixels are interpreted as the fringes.

The fringe length is calculated as the number of pixels contained by the fringe multiplied by the length of a pixel. In the case of diagonal pixels the length is calculated as $\sqrt{2}$ times the pixel size. The pixel size obviously depends on the image resolution. All fringes shorter than 0.483 nm (two aromatic ring) are eliminated. The remaining fringes are stored for further analysis. **Figure 14h** depicts the resultant fringes after the minimum length criteria filtering.

Fringe tortuosity

Tortuosity refers to the curvature of the fringe and is related to the presence of C5 rings. C5 rings allow the formation of curved carbon layers and are necessary for the formation of fullerenes and fullerenic structures [28]. Fringe tortuosity is defined as the ratio between fringe length (C) and the fringe linear length (L), represented in **Figure 15**. The fringe linear length is calculated as the Euclidean distance between the initial pixel (x_i,y_i) and final pixel (x_f,y_f):

$$L = \sqrt{(x_i - x_f)^2 + (y_i - y_f)^2} \tag{1}$$

Inter-fringe spacing

The calculation of the separation between fringes is not trivial and in the past has been

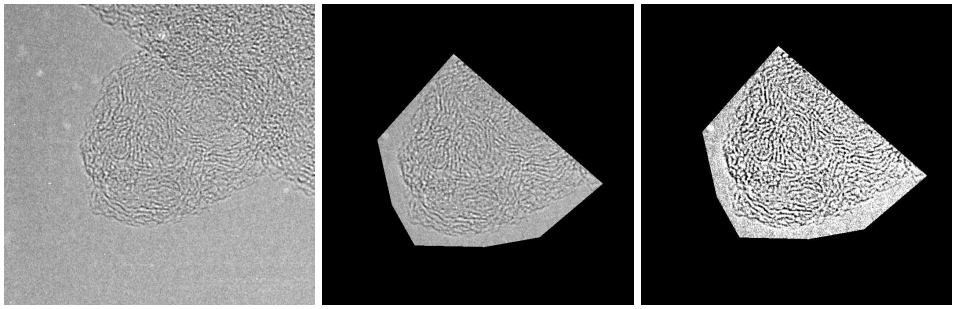

(a) *HRTEM.* **(b)** *Selection of ROI.* **(c)** *Contrast enhancement.*

(d) *Gaussian filter.* **(e)** *Bottom hat transformation.* **(f)** *Binary thresholding.*

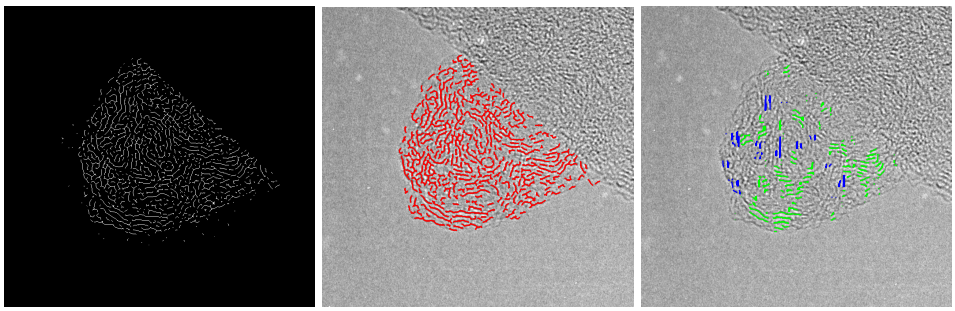

(g) *Skeletonization.* **(h)** *Selected fringes.* **(i)** *Inter-fringe analysis.*

Figure 14: *Image processing*

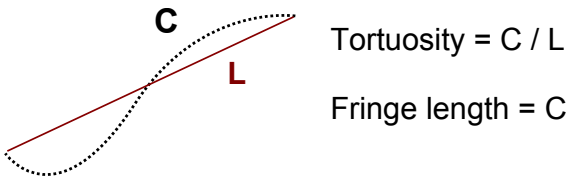

Figure 15: *Calculation of fringe length and tortuosity.*

calculated using closed-source software. *Sharma et al* [52] developed an automated algorithm to calculate inter-layer spacing in which only parallel fringes ($\pm 10^{\circ}$ inclination angle difference) with separations between 0.33-0.38 nm were considered. This eliminated a lot of fringes that were only partially parallel. *Yehliu et al* [65] developed a semi-automated algorithm to calculate the inter-layer spacing for fringes that are rela-

tively adjacent. The user selects each pair of fringes to be analysed and can trim them in order to have a pair of fringes of similar length. Although this methodology enables the consideration of more fringe pairs, is not practical. Recently an automated algorithm was presented [46] that enabled the calculation of the inter-fringe spacing based on fringe orientation and a parallelism function.

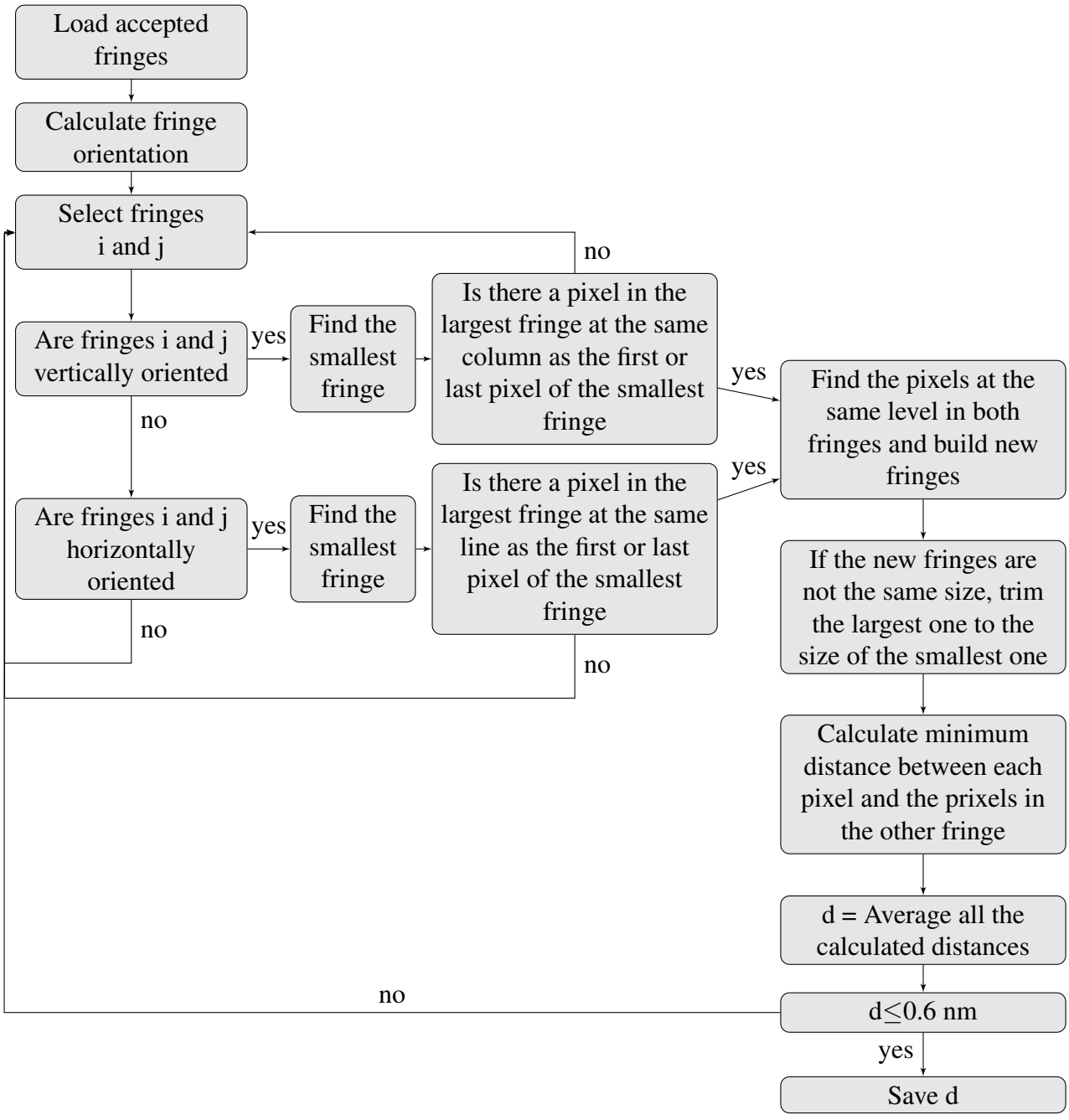

Figure 16: *Flow chart of the main steps of the inter-fringe calculation algorithm.*

In this study, an automated algorithm was developed to calculate the inter-fringe spacing represented. The algorithm is illustrated in **Figure 16**. The orientation of each fringe is calculated using the Matlab Imaging Toolbox, and can take values between -90° and

$+90°$. Two orientations were defined: 1) vertical, for fringes oriented between $+45°$ and $+90°$ or $-90°$ and $-45°$; and 2) horizontal, for fringes oriented between $-45°$ and $+45°$. All the fringes are compared to each other in terms of their orientation and pixel-to-pixel space position. If two fringes have similar orientation (vertical or horizontal) they are further analysed: All pixels in the fringes are compared in terms of their position. Those pixels which are at the same level, either vertically or horizontally depending on the orientation, are further processed. The fringes are trimmed to retain only those pixels at the same level, and to have the same length. **Figure 17** shows the selection of parallel region of fringes with different orientations. Once the sections of the two fringes that are to some extent parallel have been identified, the average of the minimum distances between the pixels is calculated as the inter-fringe distance. Only inter-fringe separations larger than the 002 graphite distance (0.3354 nm) and smaller than 0.6 nm were effectively selected. Results of the algorithm are depicted in **Figure 14i**, were the selected fringe pairs for inter-fringe spacing calculation are highlighted in blue (vertically oriented) and green (horizontally oriented).

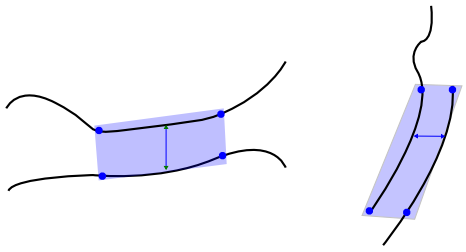

Figure 17: *Inter-fringe separation for different fringe orientation. Selection of the the parallel region of fringes with different orientations.*

B TEMSIM parameters

The selection of the optical parameters were based on the experimental setup. The SIMTEM package uses a multi-slice method to approximate the interaction between atoms and the beam. **Table 5** presents the parameters used to simulate the TEM images.

Parameter	Value
Third order spherical aberration	0 mm
Fifth order spherical aberration	1 mm
(x,y) dimension	512x512 pixel
Thickness of slice	3.5 angstrom
Beam energy	400 keV
Objective aperture	25 mrad
Magnitude of two fold astigmatism	0 angstrom
Angle of two fold astigmatism	0 degrees
Magnitude of three fold astigmatism	0 angstrom
Angle of three fold astigmatism	0 degrees
Objective lens and aperture centre (x,y)	0,0 mrad
Crystal tilt (x,y)	0,0 mrad
Incident beam tilt (x,y)	0,0 mrad

Table 5: *Parameters used for the simulation of TEM images in the TEMSIM package.*